

## AUTOPILOT DESIGN FOR A SQUARE CROSS-SECTION MISSILE

R A Hyde<sup>+</sup> & J R Cleminson<sup>\*</sup>

<sup>+</sup>The MathWorks Limited, Matrix House, Cambridge CB4 0HH, UK. [rhyde@ieee.org](mailto:rhyde@ieee.org)

<sup>\*</sup>QinetiQ Ltd, Cody Technology Park, Farnborough, Hants, GU14 0LX, UK. [jrcleminson@qinetiq.com](mailto:jrcleminson@qinetiq.com)

### ABSTRACT

Autopilots have been developed for two missile airframes. Both airframes are similar in every respect except for the cross-section of the body and the influence of this on the shape of the nose: one is circular-bodied, the other square-bodied. The square-bodied airframe, having the non-axisymmetric form, might be expected to be harder to control at higher values of angle-of-attack and sideslip, making skid-to-turn steering harder to achieve. This paper explores this and the relationship between airframe asymmetry and the required autopilot architecture to extract best stability and performance. Three autopilot designs are considered based on classical,  $H_\infty$  and NDI control approaches. Designs are compared in terms of a robust stability requirement defined by Nichols exclusion regions, which are applied in a multi-loop sense.

### INTRODUCTION

The next generation of missiles may have non-circular aerodynamic shapes for better aerodynamic performance, greater volumetric efficiency, reasons of stealth, etc. Conventional missiles with a circular cross-section have typically achieved good acceleration performance and stability margins using a classical three-loop autopilot structure. Circular cross-section airframes with an asymmetry due, for example, to an engine intake have typically relied on bank-to-turn (BTT) steering for stability reasons, and sometimes also for intake side-slip constraints. It is well understood that BTT steering is generally not as good as skid-to-turn (STT) steering in the end game. Hence, for novel airframes, it is important to understand what is the effect of cross-section shape on autopilot design and all-round-the-body stability and performance.

In this paper, we compare a square cross-section missile with a circular cross-section baseline. These are supersonic, rocket-propelled configurations, and are illustrated in Figure 1. Computational fluid dynamics was used to generate aerodynamic data at Mach 2.5 over total incid-

ence values up to  $24^\circ$  and aerodynamic roll angles between  $\pm 180^\circ$  [1]. The data were validated against experiment and good agreement was obtained.

There is not a large amount published work on the control of non-circular cross-section airframes. Work has been reported on lifting body airframes with highly elliptical cross-section [2], as well as on triangular, or triangular-like airframes [3,4]. Because of their shapes, such airframes are difficult to evaluate rigorously against traditional four-fin circular cross-section configurations. Moreover, the control solutions for them have tended to presume BTT steering to keep aerodynamic cross-coupling to a minimum [5,6,7].

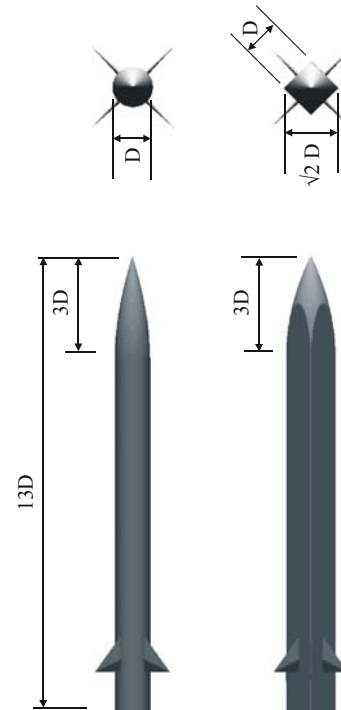


**Figure 1: Configurations of the circular and square cross-section airframes**

A number of design methods have been used to design autopilots for the two airframes. This is to help gain an understanding of how the autopilot

architecture should depend on the aerodynamics. A square cross-section body is likely to introduce additional cross-couplings that may require an autopilot architecture that mirrors these. The classical three-loop autopilot structure does not readily permit this. Of the designs considered, three are presented here:

- A classical autopilot designed using pole placement.
- A classical autopilot with an  $H_\infty$  fine-tuning compensator.
- A Non-linear Dynamic Inversion (NDI) autopilot.

This paper makes two main contributions. The first is the comparison of different cross-sectional airframes and their impact on autopilot design and the effective time constant. Secondly, additional insight into the design methods themselves is given. Non-linear Dynamic Inversion is often promoted as a straightforward way to simplify the autopilot design for cross-coupled airframes. However, there is some uncertainty as to whether inverting dynamics will result in a robust architecture. The comparison of the NDI design with the classical and  $H_\infty$  designs provides some new insight on this.

Other aspects of the work not reported here include additional autopilot designs, steering laws and reach capability. These will be addressed in a more complete journal paper submission.

### DESIGN REQUIREMENTS

The design objective is to maximise speed of response, as measured by lateral acceleration rise-time, subject to obtaining a minimum level of stability. This minimum level of stability is defined in terms of the elliptical Nichols exclusion region shown in Figure 2. The region defines the uncertainties to be applied to all three feedback loops simultaneously. The closed-loop should remain stable in the face of these multiple uncertainties.

The exclusion region is an approximation to the conventional ones used for fixed wing military aircraft [8], an example of which is also shown in Figure 2. The use of straight edges is somewhat arbitrary, and does not lend itself to automated analysis as well as an ellipse. The ellipse in Figure 2 is defined by:

$$r = \frac{1 + \delta}{1 - \delta} \quad \text{Equation 1}$$

where  $\delta$  is a complex number bounded in size by  $|\delta| < c$ , and  $c$  is a constant real number.

Substituting  $\delta = ce^{j\theta}$  (where  $j = \sqrt{-1}$ ), and varying  $\theta$  between 0 and  $2\pi$  results in  $r$  tracing out the ellipse. By choosing the value of  $c$  appropriately, the ellipse can be made to approximate the conventional region based on straight edges. A value of  $c=0.25$  was used here, as this is commonly accepted as reasonable for multivariable analysis. It is equivalent to roughly 4.5dB and  $30^\circ$  in the principal directions. The reduced margins are afforded in multivariable analysis because cross-coupling and simultaneous offsets are explicitly accounted for.

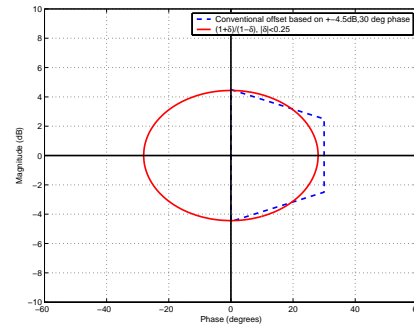


Figure 2: Nichols exclusion regions

With the exclusion region parameterized in this way, stability analysis can be turned into a  $\mu$ -analysis task. For more detail on the method of  $\mu$ -analysis, reference [9] is a good starting point. Here, the transformation into an equivalent  $\mu$ -analysis task is shown only. Consider the block diagram in Figure 3. Writing down the relationship between  $e$  and  $u$  gives Equation 1.

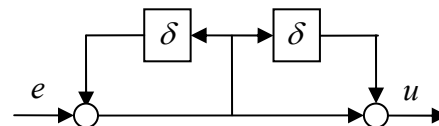
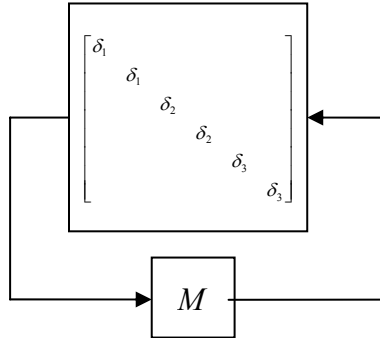


Figure 3: Modelling actuator uncertainty

If there are three primary actuator demands (i.e. the collective demands in roll, pitch and yaw), then three of the block-diagram constructions shown in Figure 3 are added to the total

interconnection structure. Pulling the six  $\delta$ -blocks out of the interconnection structure results in the diagram in Figure 4.



**Figure 4: Uncertainty applied to three primary actuator demands**

This is now in a format suitable for  $\mu$ -analysis, the uncertainty structure being three repeated complex blocks of size two. For this uncertainty structure, with  $c=0.25$ , the structured singular value ( $\mu$ ) needs to be less than 4 at all frequencies. Then there are no values of  $\delta_1, \delta_2, \delta_3$  bounded by  $|\delta_i| < 0.25$  that destabilise the closed loop. In this paper, the multivariable stability margin is plotted. This is denoted  $\varepsilon_\mu$  and defined as the minimum value, over frequency, of  $1/\mu$ . Accordingly, the aim for robust stability is  $\varepsilon_\mu > 0.25$ .

In order to ensure some realism when designing the autopilot gains, it was assumed that the gain when breaking the feedback loop at the collective pitch and yaw demands, must be less than -25dB at 50Hz. In the roll loop, the value was -25dB at 75Hz. These constraints were imposed to limit structural coupling problems via the inertial instruments.

### MISSILE DYNAMICS

As Fig 1 shows, both airframes have the same length and the diameter of the circular cross-section is equal to the side-length of the square, i.e. the circular cross-section just fits inside the square. Also, because they are side-mounted, the fins of the square cross-section airframe are identical in shape, size and arrangement to those of the circular. In both missiles, fin actuation was given second-order lag representation of un-

damped natural frequency 30Hz and damping of 0.7. For easier comparisons, the two airframes were assumed to have the same mass and the same inertias. This corresponds approximately to the (not necessarily unrealistic) situation where the internals of the square are the same as those of the circular. All analyses in this paper are for a Mach number of 2.5, total incidences up to 24°, and an altitude of 10km.

It is of interest to examine the natural stability of the airframes via the state space. Equations 2 and 3 are the state equations for the circular and square airframes at the particular trim case where the angles of attack and sideslip are both 12°, i.e. total incidence of 17° and aerodynamic roll angle of 45°. This condition is fairly close to the maximum trim capability of the circular. In the case of the circular airframe, the eigenvalues are  $\pm 22, -0.39$  and  $-0.35 \pm 15j$ . In the square case they are  $-0.016, -0.56 \pm 23j$  and  $-0.51 \pm 17j$ .

$$\begin{bmatrix} \dot{p} \\ \dot{q} \\ \dot{r} \\ \dot{v} \\ \dot{w} \end{bmatrix} = \begin{bmatrix} 0 & 0 & 0 & 1.6100 & -1.6100 \\ -0.08000 & 0 & 0 & -0.1501 & -0.1681 \\ -0.08000 & 0 & 0 & 0.1681 & 0.1501 \\ 152.6 & 0 & -717.9 & -0.5502 & -0.1581 \\ -152.6 & 717.9 & 0 & -0.1581 & -0.5502 \end{bmatrix} \begin{bmatrix} p \\ q \\ r \\ v \\ w \end{bmatrix} + \mathbf{B} \begin{bmatrix} \varepsilon \\ \eta \\ \zeta \end{bmatrix}$$

Equation 2

$$\begin{bmatrix} \dot{p} \\ \dot{q} \\ \dot{r} \\ \dot{v} \\ \dot{w} \end{bmatrix} = \begin{bmatrix} 0 & 0 & 0 & -0.06433 & 0.06433 \\ -0.08932 & 0 & 0 & 0.1439 & -0.5549 \\ -0.08932 & 0 & 0 & 0.5549 & -0.1439 \\ 152.6 & 0 & -717.9 & -1.077 & 0.05988 \\ -152.6 & 717.9 & 0 & 0.05988 & -1.077 \end{bmatrix} \begin{bmatrix} p \\ q \\ r \\ v \\ w \end{bmatrix} + \mathbf{B} \begin{bmatrix} \varepsilon \\ \eta \\ \zeta \end{bmatrix}$$

Equation 3

Cross-coupling from the roll channel into incidence ( $v$  and  $w$ ), and back the other way, is clearly evident from Equations 2 and 3. It is this cross-coupling that is the source of the fast unstable pole. This can be verified by changing the signs of the elements  $\{1,4\}$  and  $\{1,5\}$  of the A-matrix. The effect is to change the eigenvalues for the circular case to  $-0.37, -0.013 \pm 22j$  and  $-0.35 \pm 15j$  and for the square case to  $0.017, -0.58 \pm 22j$  and  $-0.59 \pm 17j$ . These elements are proportional respectively to  $\partial C_\ell / \partial \beta$  and  $\partial C_\ell / \partial \alpha$ , i.e. they represent the slopes of the aerodynamic roll moment with incidence.

Figure 5 shows the fins-undeflected rolling moment coefficients. The same non-dimensionalising factor is used in both cases, so the plots are directly comparable. The natural instability of the circular airframe tends to be

fastest at the higher incidences around the aerodynamic roll angles of  $\pm 45^\circ$  and  $\pm 135^\circ$ . These occur where the slopes of the fins-undeflected rolling moments are at their most adverse. A similar relationship holds for the square airframe, this time with natural instability being fastest at the higher incidences around  $0^\circ$ ,  $\pm 90^\circ$  and  $\pm 180^\circ$ . The only regions of complete natural stability for the fully coupled circular airframe are around mid-incidence close to the control-frame pitch and yaw directions. For the fully coupled square airframe, in contrast, complete natural stability is achieved only at some of the higher incidences around the aerodynamic roll angles of  $\pm 45^\circ$  and  $\pm 135^\circ$  – where the circular airframe exhibits its fastest instability. These characteristics strongly influence the stability margins that are achieved with the autopilots.

### CLASSICAL AUTOPILOT

Figure 6 shows the classical autopilot architecture, which follows [10]. Note that the scaling required on reference demands for zero steady-state tracking is not shown. Each channel is designed separately using pole-placement to achieve the desired time responses. This is done with just the airframe states. Adding an integrator gives a third-order system in each case, the closed-loop poles of which are assigned to desired values. Then actuator and sensor dynamics are added, and the achieved pole locations are examined. If these locations are too far away from those demanded, or if the structural attenuation constraints are being violated, the demanded pole locations are revised and the process is repeated.

### $H_\infty$ AUTOPILOTS

Design using the  $H_\infty$  method covers a number of approaches. Here, we use the  $H_\infty$  Loop-Shaping Design Procedure (LSDP) [11,12] to fine-tune the classical design. Figure 7 shows the closed-loop feedback structure for LSDP.  $G$  is the missile airframe with the three collective fin demands as inputs, and three gyros and two accelerometers as outputs.  $W_1$  and  $W_2$  are diagonal weighting matrices chosen by the designer using conventional loop-shaping objectives i.e. sufficient open-loop gain at low frequency for disturbance rejection, roll-off at high frequency for noise/structural vibration

attenuation, and suitable stability margins around gain cross-over. Given  $W_1$  and  $W_2$ , the optimal  $H_\infty$  loop-shaping compensator,  $K_\infty$ , is then synthesised. This optimisation makes the shaped plant,  $W_2GW_1$ , as robust as possible to normalised coprime factor uncertainty (see [11] for the definition). The bound on the smallest uncertainty that just destabilises the closed loop is denoted  $\mathcal{E}_{ncf}$  in this paper.

It has been shown in [13] that this type of uncertainty is equivalent to that defined in Figure 4, but applied to both plant inputs and outputs simultaneously. Hence, making the closed-loop robust to normalised coprime factor uncertainty should provide some level of guarantee of robustness to the case where all the uncertainty is defined at the actuators.

For the design here, the classical autopilot is taken to be the weight  $W_2$ , and  $W_1$  is set to the identity matrix as shown in Figure 8. Hence the  $H_\infty$  compensator is used to fine-tune the loop-shapes at the actuators, adding cross-terms as necessary to achieve good robustness to normalised coprime factor uncertainty.

### NON-LINEAR DYNAMIC INVERSION

The notion of NDI has existed for many years: see for example [14,15]. The method essentially inverts the system dynamics up to some specified frequency i.e. the desired closed-loop bandwidth. An advantage of the NDI approach is that no separate gain scheduling is required, thereby making its implementation more straightforward. It also incorporates knowledge of the non-linear system into the design, and hence it might be expected that better performance could be achieved. A disadvantage is that it does not directly address robust stability, and hence the stability-performance trade-off is not easily made. One approach to mitigate this is proposed in [16] whereby the NDI method is combined with simple lead-lag inner-loop compensation scheme designed with the aid of coprime factor based stability analysis.

The missile airframe equations can be written in the form:

$$\dot{x} = F(x) + G(x, u)$$

For NDI, the usual assumption is that the equations are linear in the control i.e.

$$\dot{x} = F(x) + G(x)u$$

In many, if not most, papers on NDI with reference to missiles, writing in this form does not present a problem. This is typically because the application uses BTT steering, and correspondingly side-slip is maintained around zero. As a result, fin cross-coupling terms are small. For the missiles studied here this is not the case, as relatively large simultaneous angles of attack and sideslip are to be achieved. Expanding on the specific terms in  $x$  and  $u$  on which the control term depends gives:

$$\dot{x} = F(x) + G(\sigma, \lambda, \zeta, \eta, \xi)$$

Hence inversion involves finding and implementing a five-dimensional table with desired moments ( $L, M, N$ ) and current incidence values as inputs, and the roll, pitch and yaw collective fin demands as outputs. Note that inversion does not result in equations that are linear in the control, but this does not prevent the assignment of the closed-loop dynamics to some desired set of values.

Figure 9 shows the autopilot architecture. The inner loop contains an NDI controller for roll, pitch and yaw control. An outer classical architecture is used for acceleration tracking. Initially an outer loop NDI controller was also tried using the time-scale separation approach proposed in [17]. However, it was found that faster acceleration responses were possible with the classical outer loop. With the NDI inner-loop providing fast decoupled roll, pitch and yaw control, there is less need for a complex outer loop.

The outer loop acceleration and synthetic gains are set to achieve desired speed of response and less than 2% overshoot. The inner-loop demanded bandwidths  $\omega_p, \omega_q$  and  $\omega_r$  are made as fast as possible whilst respecting the required stability margin,  $\varepsilon_\mu$ . The procedure used for design is:

1. Postulate values for  $\omega_p, \omega_q$ , and  $\omega_r$ .
2. Design the outer loop to achieve desired rise time and overshoot.
3. Calculate  $\varepsilon_\mu$ . If  $\varepsilon_\mu$  is too small, revise set of values for  $\omega_p, \omega_q$  and  $\omega_r$  (and possibly

the desired rise time if necessary), and then repeat steps 1 to 3.

Pushing the inner loop desired bandwidths too high results in poor robustness due to the cumulative phase lag of actuators, sensors and short period mode. Conversely, making them too low results in failure to damp the short-period modes adequately and/or stabilise the unstable roll modes. Similarly, too aggressive an acceleration time response adversely affects stability margins.

The inner-loop NDI is based on the following moment equations:

$$J\dot{\Omega} + J\hat{\Omega} = (x_{aero} - x_{cg}) \wedge S_{ref} \bar{q} \begin{bmatrix} C_{X_{body}} \\ C_{Y_{body}} \\ C_{Z_{body}} \end{bmatrix} + S_{ref} d_{ref} \bar{q} \begin{bmatrix} C_{L_{body}} \\ C_{M_{body}} \\ C_{N_{body}} \end{bmatrix} + S_{ref} d_{ref} \bar{q} \begin{bmatrix} C_{L_{fin}} \\ C_{M_{fin}} \\ C_{N_{fin}} \end{bmatrix}$$

Assigning the desired closed-loop dynamics with

$$\hat{\Omega} = \begin{bmatrix} \omega_p(p_d - p) \\ \omega_q(q_d - q) \\ \omega_r(r_d - r) \end{bmatrix} \text{ and rearranging gives the desired}$$

fin moment coefficients as:

$$\begin{bmatrix} C_{L_{fin}} \\ C_{M_{fin}} \\ C_{N_{fin}} \end{bmatrix} = \frac{1}{S_{ref} d_{ref} \bar{q}} J \begin{bmatrix} \omega_p(p_d - p) \\ \omega_q(q_d - q) \\ \omega_r(r_d - r) \end{bmatrix} + \frac{1}{S_{ref} d_{ref} \bar{q}} J \hat{\Omega} - \frac{(x_{aero} - x_{cg}) \wedge \begin{bmatrix} C_{X_{body}} \\ C_{Y_{body}} \\ C_{Z_{body}} \end{bmatrix}}{d_{ref}} - \begin{bmatrix} C_{L_{body}} \\ C_{M_{body}} \\ C_{N_{body}} \end{bmatrix}$$

These desired moments are converted to collective fin demands by off-line inversion of the aerodynamics, and are implemented as a 5-dimensional look-up table.

An second NDI design based on the transformed equations of motion in the parameter varying form proposed in [18] was also investigated, but is not reported on here. Comparable results were obtained.

## ROBUSTNESS ANALYSIS

Figure 10 shows the robustness analysis results, as measured by  $\varepsilon_\mu$ , for each of the designs.

Only the  $H_\infty$  autopilots meet the criterion of  $\varepsilon_\mu > 0.25$ , but the NDI autopilots are close to achieving it. There are two contributing trends to

the designs that fail the criterion. The first is a gradual decrease in achieved robustness with total incidence. The second is an undulation with aerodynamic roll angle, which becomes more pronounced at higher total incidence.

The first trend can be attributed to compensator order afforded by the design method. The fast unstable pole in roll must be stabilised via a feedback loop with sufficient bandwidth. The NDI and classical autopilots, being of restricted order, are less able than the  $H_\infty$  designs to introduce shaping at cross-over to counter the lag of the actuators and satisfy the structural attenuation constraint. A secondary factor is the restriction on permissible autopilot cross terms. The classical design does not have them. The NDI controller does, but they are chosen on the desire to invert the nominal dynamics, not on the basis of robustness.

The undulation in achieved stability with aerodynamic roll angle is directly related to the fast unstable pole in roll, which in turn depends on the slope of the fins-undeflected roll coefficient, illustrated in Figure 5. The dips in robustness correspond to where the unstable pole is the fastest. This undulation is much more pronounced for the square airframe, and the trend of the results suggests that it would be much worse at higher total incidence values than those considered here.

From the analysis, the following may be concluded:

- Even for a circular cross-section, cross-axis coupling requires a more complex architecture than that afforded by the classical three-loop structure, if operation using STT steering is required at higher incidence levels.
- Over the incidence range considered, the square airframe is not significantly harder than the circular airframe to control. However, for higher incidence values than those considered, this is not expected to be the case.
- The reduced stability margins achieved by the NDI design are most likely due to the inability of the method to add higher order dynamics. Its inherent inversion of the control may also be a contributing factor.

## TIME DOMAIN ANALYSIS

Figure 11 shows plots of the effective time-constant as defined as the time for which:

$$1 - \sqrt{(\bar{y} - \bar{y}_c)^2 + (\bar{z} - \bar{z}_c)^2} = 0.63$$

where

$$\bar{z}_c = z_c / \sqrt{z_c^2 + y_c^2}$$

$$\bar{y}_c = y_c / \sqrt{z_c^2 + y_c^2}$$

$$\bar{z} = z / \sqrt{z_c^2 + y_c^2}$$

$$\bar{y} = y / \sqrt{z_c^2 + y_c^2}$$

and  $[z_c, y_c]$  and  $[z, y]$  denote commanded and achieved accelerations. This measure is thus the time taken to reach 63% of demanded acceleration, taking into account both acceleration magnitude and direction. Note that this is a more general definition than is required for STT steering.

All designs show a reasonably consistent time constant. Some variation is expected due to the airframe shape. For example, this is clearly visible for the first plot for the square case. Interestingly, the NDI shows least variation, possibly reflecting that it takes better account of the non-linear system equations.

## CONCLUSIONS

The objective of this study was to understand if an airframe with square cross-section body might present additional complexities for autopilot design, and result in compromised stability or performance. From the analysis undertaken, indications are that such a missile can be adequately controlled for the purposes of STT steering, at least for the conditions considered, i.e. Mach 2.5 and total incidences up to 24°. Nevertheless, the increased undulation in achieved stability margins for the square cross-section airframe is likely to present more of a problem should STT operation at significantly higher total incidences be required.

The work has provided additional insight into the autopilot design methods. For both airframes, the classical three-loop autopilot does not provide the necessary architecture in terms of cross-terms. Accordingly, stability margins are necessarily compromised at higher incidence levels.

The NDI method, despite including the non-linear dynamics in the design process, performed marginally worse than the  $H_\infty$  approach. A more systematic means of inverting the control moments and of manipulating the high-frequency behaviour of the NDI autopilot are required.

More details of this work, including variations on the autopilots presented here, alternative steering laws, trim capability and other agility metrics are contained in a journal paper to be submitted shortly.

### **ACKNOWLEDGEMENTS**

This work was funded by the Energy, Guidance and Control Domain of the UK MOD Corporate Research Programme. The authors would also like to thank Trevor Birch, of the UK MOD Defence Scientific and Technical Labs, and Ian Moule and Mark Wood, both of QinetiQ Bedford, who generated the aerodynamic data and offered helpful advice.

### **REFERENCES**

[1] Birch, T and Cleminson, J.R. "Aerodynamic Characteristics of a Square Cross-Section Missile Configuration", ref. AIAA-2004-5197, AIAA 22<sup>nd</sup> Applied Aerodynamics Conference, Rhode Island, August 2004.

[2] McGehee, R.M., and Emmert, R.I., "Bank-to-turn (BTT) Autopilot Technology," *Proceedings of the IEEE National Aerospace and Electronics Conference*, Vol. 2., 1978.

[3] Huber, A., Ford K., Mook, R., and Woods, D., "Havedash 2: development test and evaluation of an advanced air-to-air missile concept," *Proceedings of 36<sup>th</sup> Symposium of Experimental Test Pilots*, 1992.

[4] Agrell, J., Hamnér, and O., Jonsson, B., "Aerodynamics of missiles with triangular cross-sections," *Proceedings of the 21<sup>st</sup> ICAS Congress*, Melbourne, Australia, September 1998.

[5] Lee, K.L., Langehough, M.A. and Chamberlain Capt R.A. "Modern bank-to-turn autopilot for Have Dash II missile", IEEE Conference on Control Applications, 1992.

[6] Schumacher, C. and Khargonekar, P. "Missile autopilot design using  $H_\infty$  control with gain scheduling and dynamic inversion", Journal

of Guidance, Control and Dynamics, 21(2):234-243, 1998.

[7] Halsey, K.M. "Nested Feedback Systems", PhD thesis, Department of Engineering, University of Cambridge, September 2002.

[8] Korte, U. "The Industrial Process for Clearance of Flight Control Laws of Fighter Aircraft", GARTEUR Technical Report TP-119-6, FM(AG11), 21<sup>st</sup> January 2000.

[9] Packard, A. and Doyle, J., "The complex structured singular value," *Automatica*, Vol. 29, Issue 1, pp. 71-109, 1993.

[10] Nesline, F.W. & Nesline M.L., "How autopilots constrain the aerodynamic design of homing missiles", American Control Conference, 1984.

[11] McFarlane, D.C. and Glover, K. "Robust Controller Design Using Normalised Coprime Factor Plant Descriptions", Lecture Notes in Control and Information Sciences, Springer-Verlag, 1990.

[12] Hyde, R.A. " $H_\infty$  Aerospace Control Design – A VSTOL Flight Application", Advances in Industrial Control Series, Springer-Verlag, 1995.

[13] Glover, K, Vinnicombe, G, and Papageorgiou, G. "Guaranteed Multi-Loop Stability Margins and the Gap Metric" Proceedings of the IEEE 39th Conference on Decision and Control, Sydney, Dec 2000.

[14] Snell, S.A., Enns, D.F. and Garrard, W.L. "Nonlinear Inversion Flight Control Law for a Supermaneuverable Aircraft", AIAA-90-3406-CP.

[15] "Application of Multivariable Control Theory to Aircraft Control Laws", Honeywell Technology Center and Lockheed Martin Skunk Works, published by Wright-Patterson Air Force Base ref WL-TR-96-3099, May 1996.

[16] G. Papageorgiou & R.A. Hyde "Analysing the stability of NDI-based flight controllers with LPV methods", *Proceedings of the AIAA Guidance, Navigation and Control Conference*, Montreal, 2001.

[17] Menon, P.K. , Iragavarapu, V.R., Ohlmeyer, E.J. "Nonlinear Missile Autopilot Design Using Time-Scale Separation", AIAA-97-3765, 1997.

[18] Shamma, J.S. and Cloutier, J.R. "Gain Scheduled Missile Autopilot Design using Linear Parameter Varying Transformations", *Journal of Guidance, Control and Dynamics*, Volume 16, No. 2, March-April 1993.

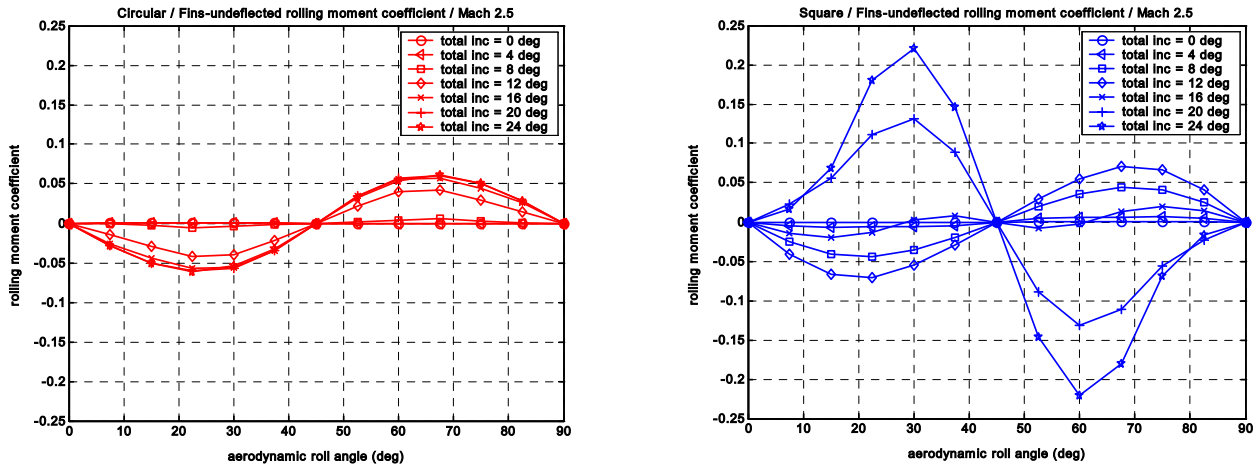


Figure 5: Circular and square airframe fins-undeflected rolling moment coefficients

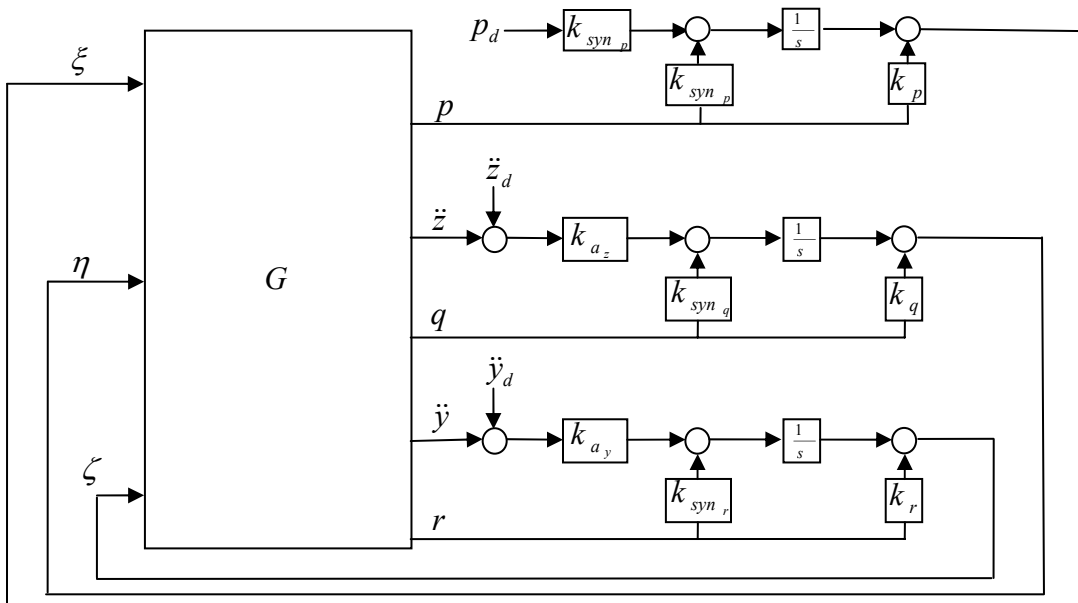


Figure 6: Classical autopilot structure

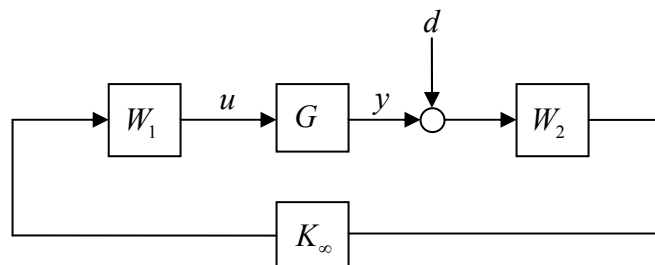


Figure 7:  $H_\infty$  loop-shaping autopilot structure

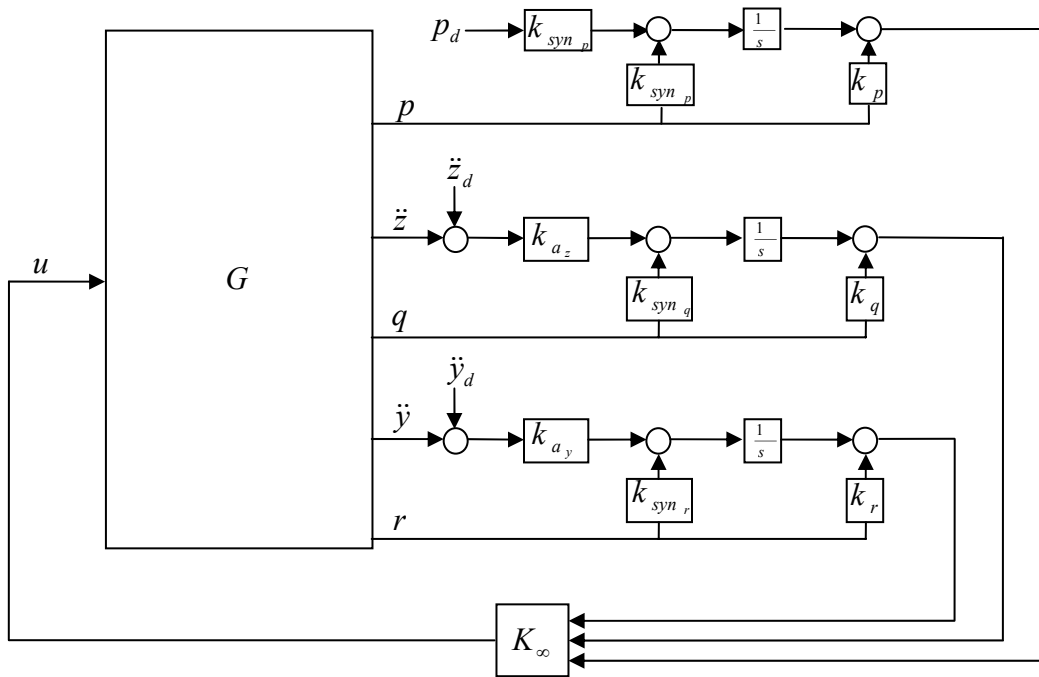


Figure 8: Classical autopilot structure plus  $H_\infty$  loop-shaping compensator

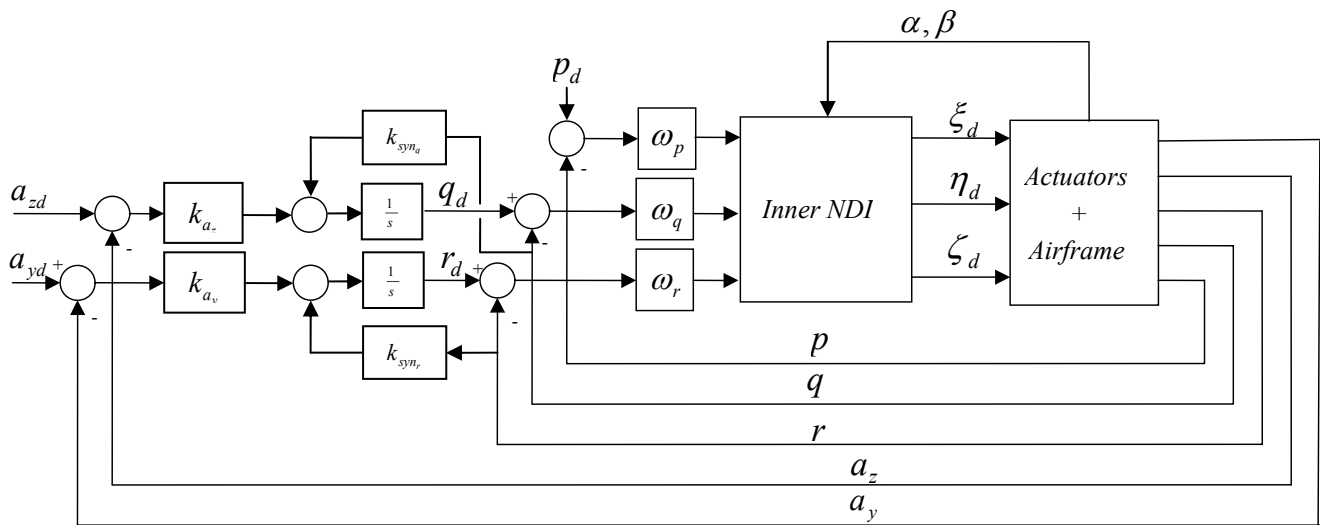


Figure 9: Inner-loop NDI autopilot plus classical outer loop

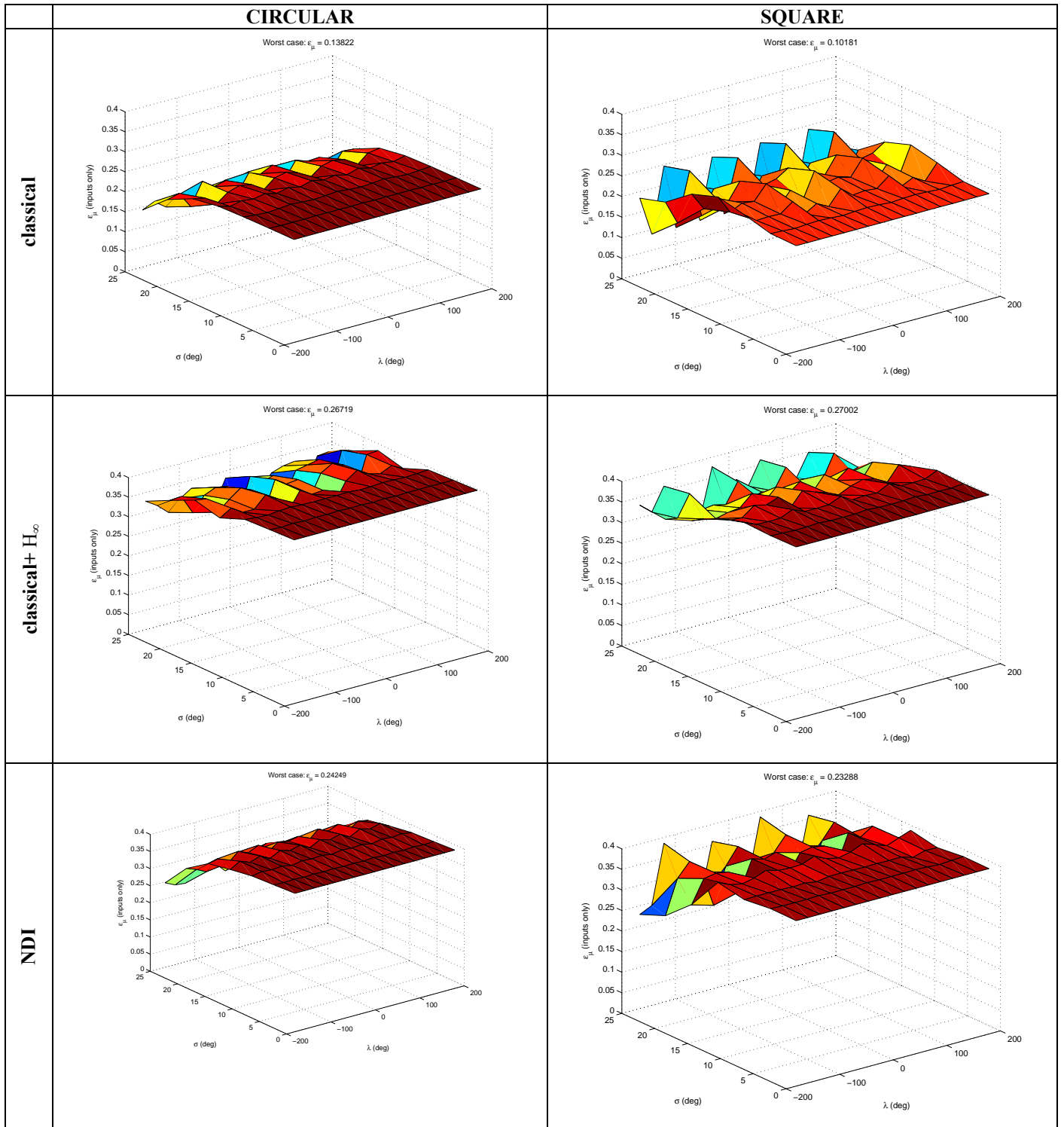
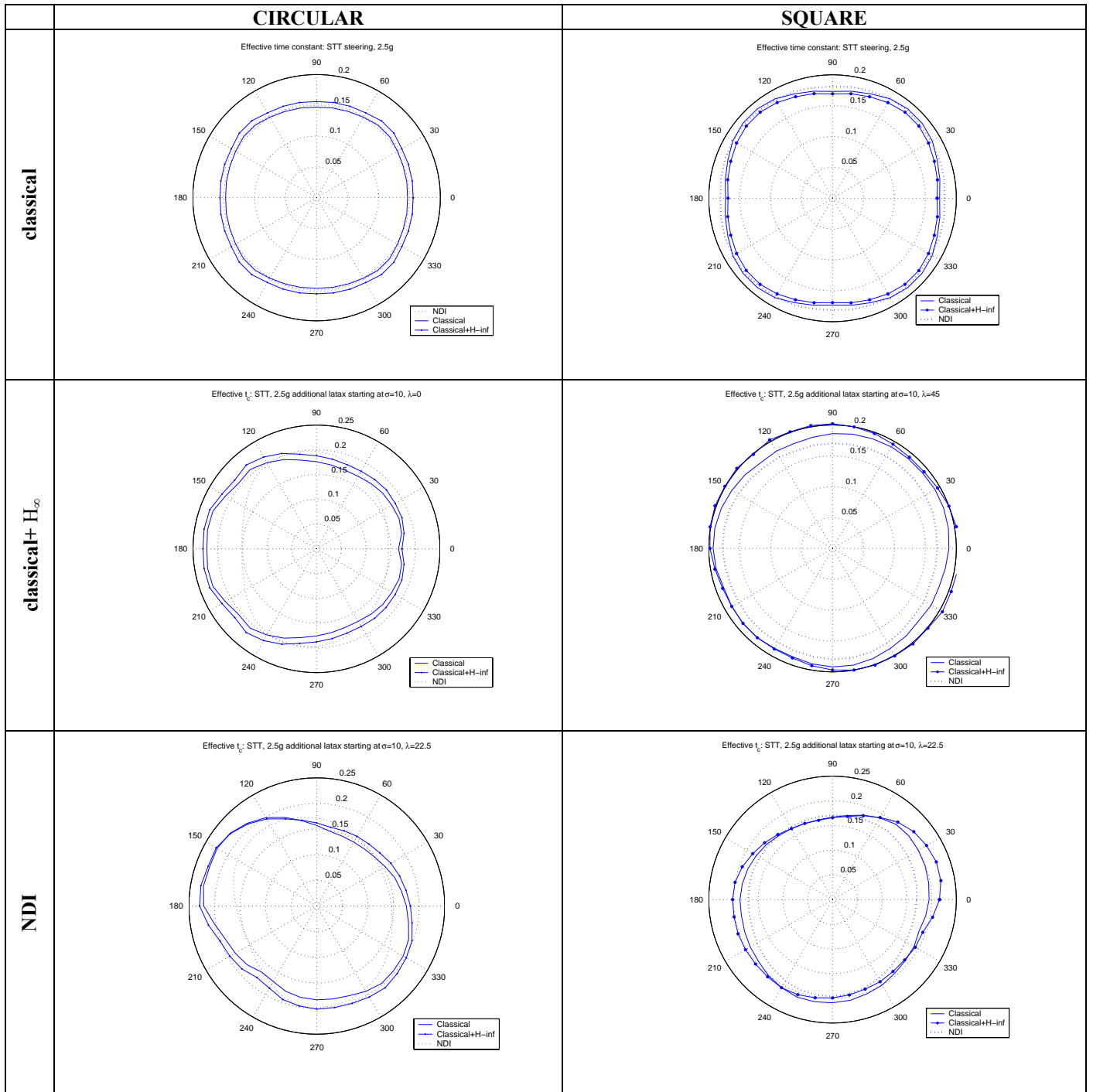


Figure 10: Robustness results as measured by  $\epsilon_\mu$



**Figure 11: Effective time constant plots**